Supporting Information

Strong Fano Resonance Excited in an Array of Nanoparticle-in-Ring Nanostructure for Dual Plasmonic Sensor Applications

Bin Ai,[†]* *Chunyuan Song*,[‡] *Layne Bradley*,[†] and *Yiping Zhao*[†]

[†]Department of Physics and Astronomy, University of Georgia, Athens, GA 30602, USA

E-mail: binai@tamu.edu

[‡]Key Laboratory for Organic Electronics and Information Displays & Jiangsu Key Laboratory for Biosensors, Institute of Advanced Materials (IAM), Jiangsu National Synergetic Innovation Center for Advanced Materials (SICAM), Nanjing University of Posts & Telecommunications, Nanjing 210023, China.

Section S1. AFM Profiles of TRA

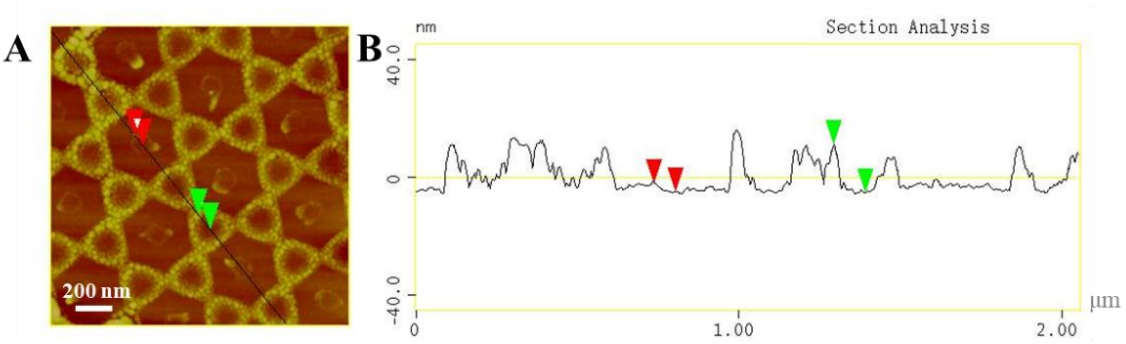

Figure S1. (A) A representative AFM image of TRA. (B) Cross-section analysis along the black line in (A). The red and green markers indicate the thickness of the PS residue (3 nm) and TRA (16 nm), respectively.

Section S2. AFM Images of the Ag Patterns with θ_2 = 7.5° and 10°

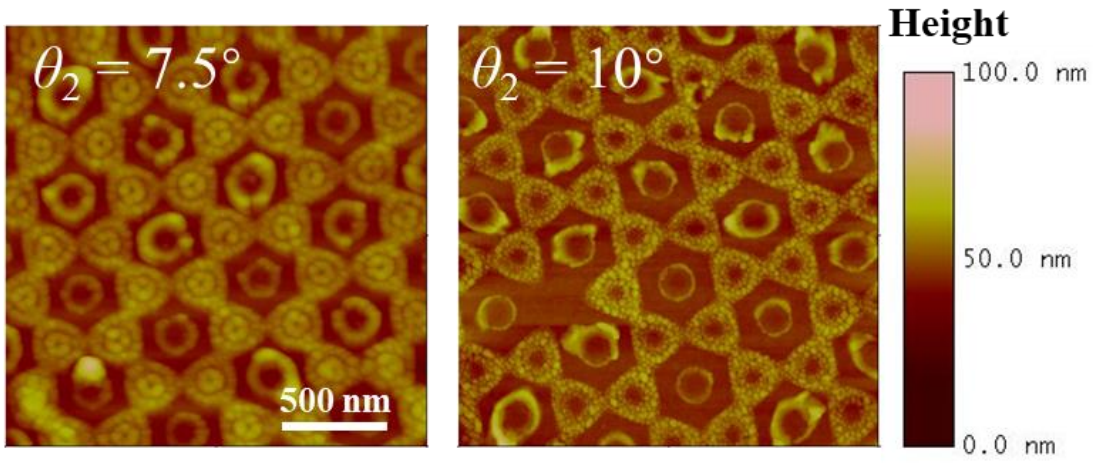

Figure S2. Representative AFM images of the Ag patterns fabricated with θ_2 = 7.5° and 10°.

As shown in Figure S2, a circular ring with a small hole was formed in the center of the triangular ring when θ_2 = 7.5°. When θ_2 = 10°, the inner ring became larger, and it merged with the triangular ring. Thus, no nanoparticles (NPs) and gaps were observed in the triangular ring.

Section S3. Quantitative Analysis of the Spectra

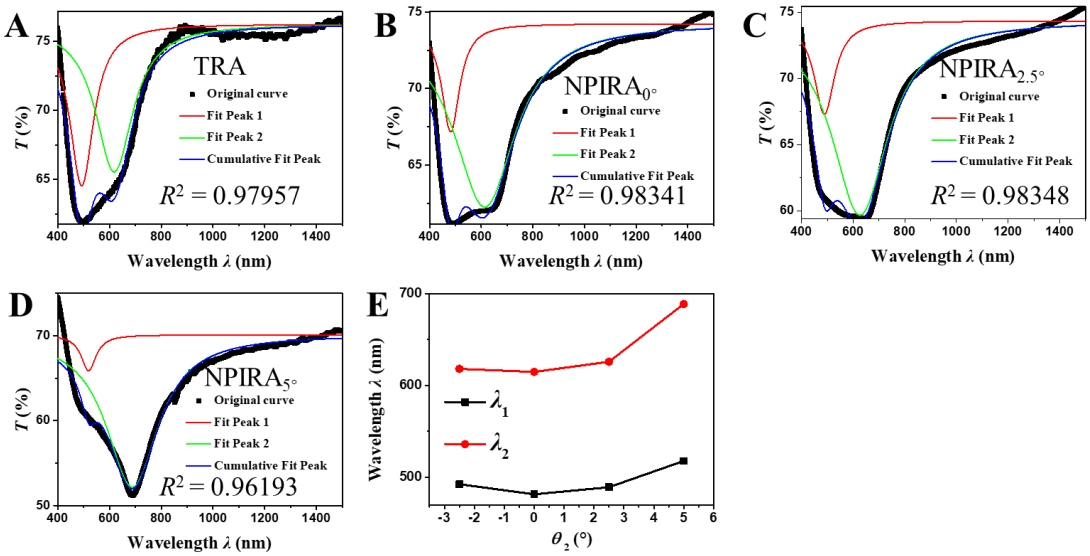

Figure S3. Lorentz function fitting of the transmission spectra of (A) TRA, (B) NPIRA$_{0°}$, (C) NPIRA$_{2.5°}$, and (D) NPIRA$_{5°}$. (E) Plots of the wavelength of λ_1 and λ_2 versus θ_2. θ_2 = - 2.5° represents the TRA sample.

The transmission spectra were fitted by a linear combination of Lorentz functions, as shown in Figures S3A-3D. The coefficient of determination (R^2, a number that indicates the proportion of the variance in the dependent variable that is predictable from the independent variable) is shown in each figure, manifesting the good quality of the fitting.

Section S4. FDTD Calculation Model

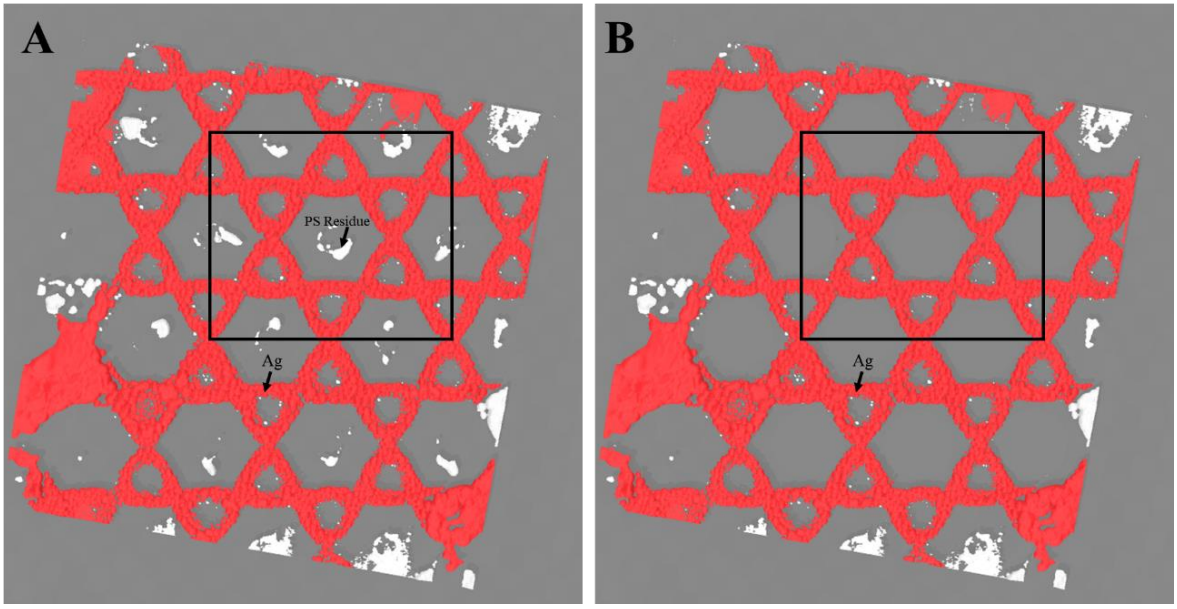

Figure S4. Schematics of the FDTD model (A) with the PS residue and (B) after removing the PS residue.

Figure S4A shows an example (inside black box) of the model used in FDTD. The AFM image of TRA with an area of 2 × 2 μm^2 was imported to the commercial FDTD software. Two unit cells (indicated by the black rectangle) were used for the calculation area. In addition, the PS residue (white area) can be removed artificially (Figure S4B). The spectra calculated with and without the PS residue are the same, as shown in Figure 3A.

Section S5. Charge Distribution of TRA

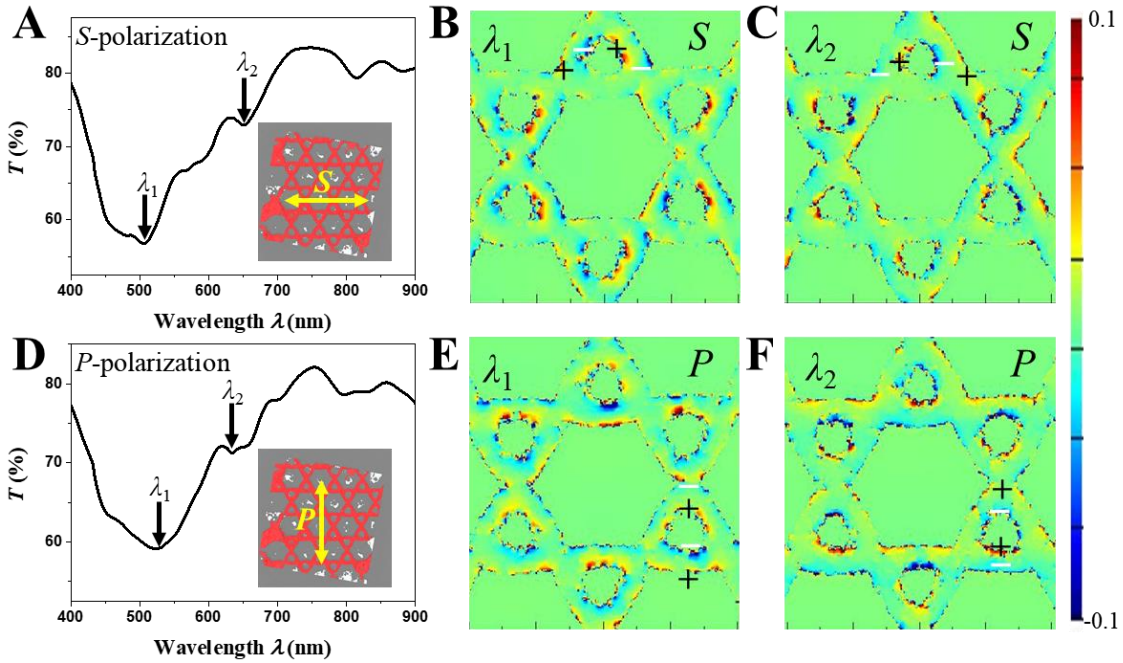

Figure S5. (A) Calculated transmission spectrum of TRA with *S*-polarization. Charge distributions were calculated at the Ag/glass interface at the wavelength of (B) λ_1 and (C) λ_2 identified in (A). (D) Calculated transmission spectrum of TRA with *P*-polarization. Charge distributions were calculated at the Ag/glass interface at the wavelength of (E) λ_1 and (F) λ_2 identified in (D).

Section S6. Local Electric Field Distributions at Resonance Wavelengths

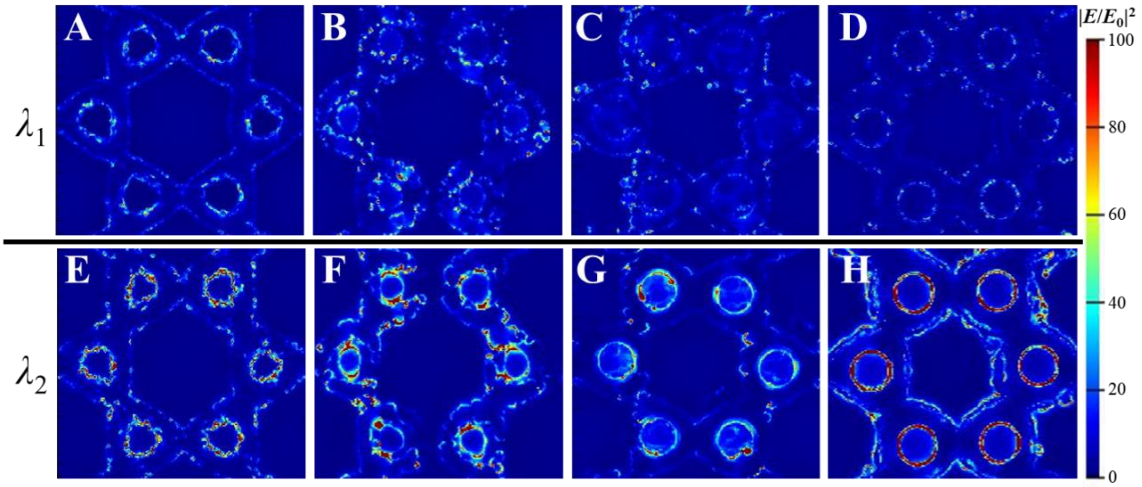

Figure S6. Local electric field distributions of the (A) TRA, (B) NPIRA$_{0°}$, (C) NPIRA$_{2.5°}$, and (D) NPIRA$_{5°}$ at λ_1 at the Ag/glass interface. Local electric field distributions of the (E) TRA, (F) NPIRA$_{0°}$, (G) NPIRA$_{2.5°}$, and (H) NPIRA$_{5°}$ at λ_2 (λ_2^4) at the Ag/glass interface.

The local electric field distributions were calculated at wavelengths of λ_1 and λ_2 of as identified on red curve in Figure 3 for nonpolarized light by taking an average of two orthogonally polarized calculations. According to previous reports, LSPR at the Ag/glass interface dominated the spectrum because of the larger RI (n = 1.5) of glass compared with that of air (n = 1).[1-2] Electric fields at the Ag/glass interface were thus shown and discussed. Sums of $|E/E_0|^2$ (S_E) of these images were calculated, as shown in Figure S7. For TRA, the electric fields at λ_1 and λ_2 both concentrate at the inner hole edge (Figure S6A and S6B), but the electric field intensity at λ_2 (S_E = 3.9 × 10^5) is larger than that at λ_1 (S_E = 1.9 × 10^5) (Figure S7). For NPIRA$_{0°}$, NPIRA$_{2.5°}$, and NPIRA$_{5°}$, the electric fields at λ_1 stay weak (Figure S6B-D) and only change slightly in the range of S_E = 1.9 - 3.5 × 10^5 (Figure S7), thus λ_1 remains in almost the same location. For λ_2 (λ_2^4), strong electric fields are confined in the gap between the NP and the ring (Figure S6F-H). S_E of Figure S6F-H increases monotonously from 3.9 × 10^5

to 1.4×10^6 with θ_2 (Figure S7), *i.e.*, with the decrease of g. Thus, λ_2 becomes prominent with θ_2.

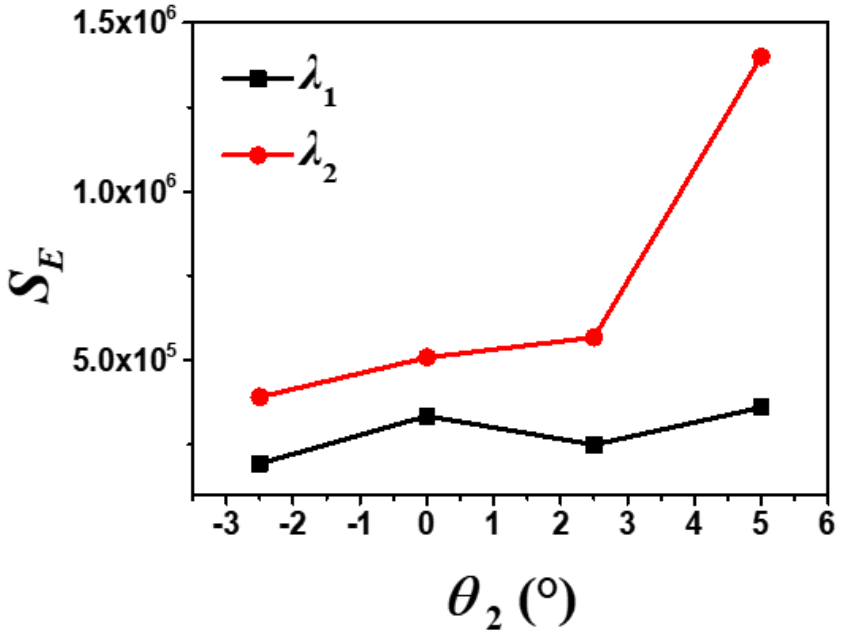

Figure S7. Plots of S_E of λ_1 and λ_2 (λ_2^4) with θ_2. θ_2 = - 2.5° represents the TRA sample.

Section S7. Charge Distribution of NPIRA$_{5^\circ}$ at λ_1

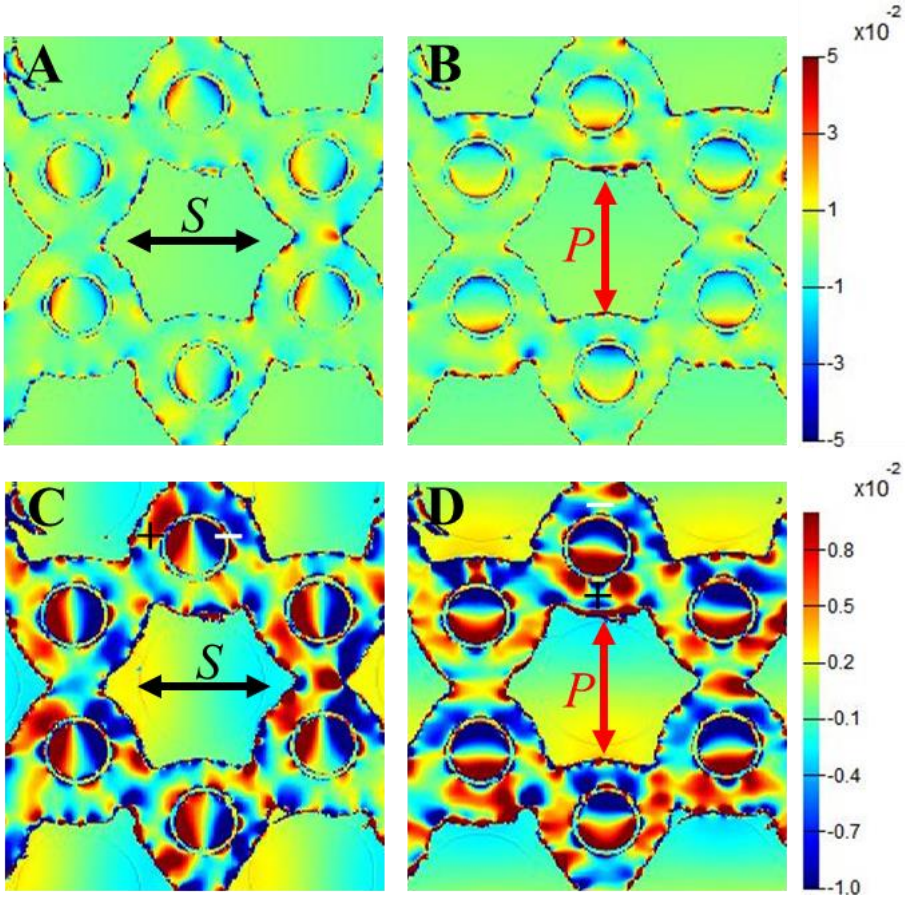

Figure S8. Charge distributions of NPIRA$_{5^\circ}$ under the (A and C) *S*- and (B and D) *P*-polarization at the Ag/glass interface at λ_1 in Figure 4A. (A) is the same as (C), and (B) is the same as (D) except that the intensity scale bars are different. The intensity scale bars of (A) and (B) are the same with those in Figure 4 for a straightforward comparison.

Section S8. Transmission Spectra of Ag Nanotriangle, Ag Nanotriangle in Ti Ring, and Ti Ring

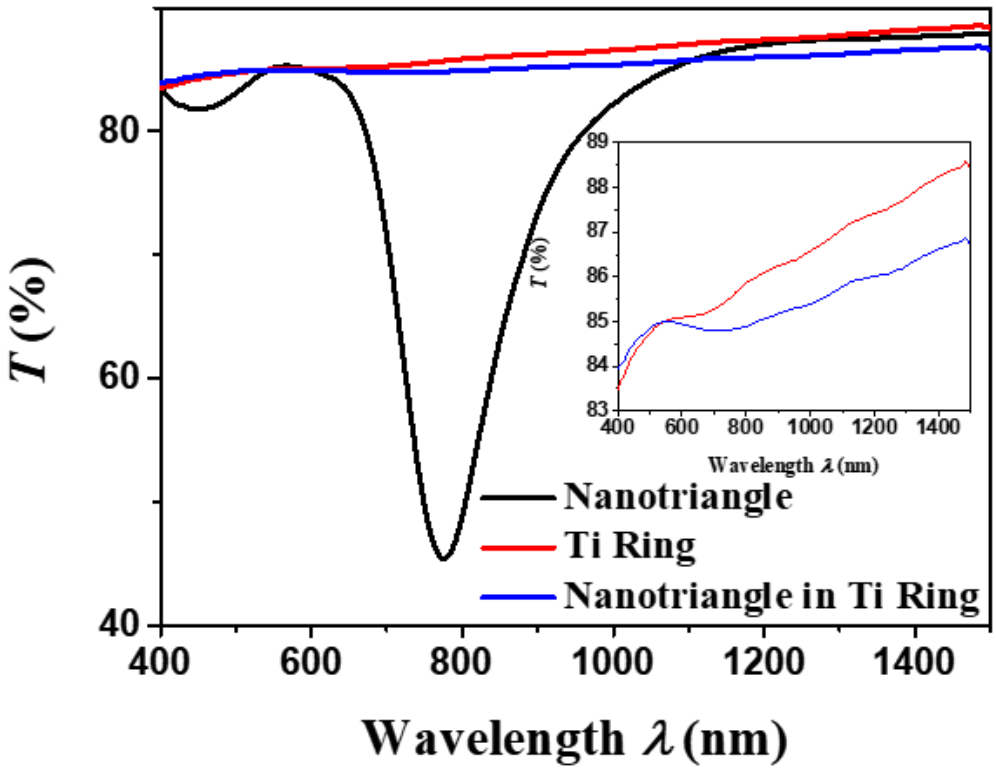

Figure S9. Transmission spectra of the Ag NP, Ag NP in Ti ring, and Ti ring.

The sample of Ag NPs was fabricated by a direct Ag deposition onto the 500-nm nanosphere monolayer at $\theta = 0°$ without rotation. A Ti ring was fabricated based on the same configuration of the first deposition in Figure 1A. After that, Ag was deposited onto the substrate based on the configuration of the second deposition in Figure 1A with $\theta_2 = 0°$, forming the Ag NPs in Ti ring. Because the mask size increased after the first deposition, the NPs in the Ti ring were smaller than the NPs directly formed by the first deposition. The structural parameters of the NP in Ti ring were the same with those of $NPIRA_{0°}$. Compared with Ag, Ti has very weak surface plasmon resonance owing to the large imaginary part of its dielectric function[3] and no obvious dips or peaks were observed for the Ti ring (blue curve). Thus, we can directly study the LSPR of the inner NP in the ring with little other resonance

interference. For the large NP, a remarkable transmission dip appeared at wavelength λ = 776 nm (black curve), which is the strong in-plane dipole LSPR on the Ag/glass interface.[4] For the smaller NPs in the Ti ring, the dipole mode would blue-shift and the absorption became weaker (red curve),[5] thus resulting in the weak transmission dip at λ = 705 nm.

Section S9. SERS of $NPIRA_{5^\circ}^{750}$

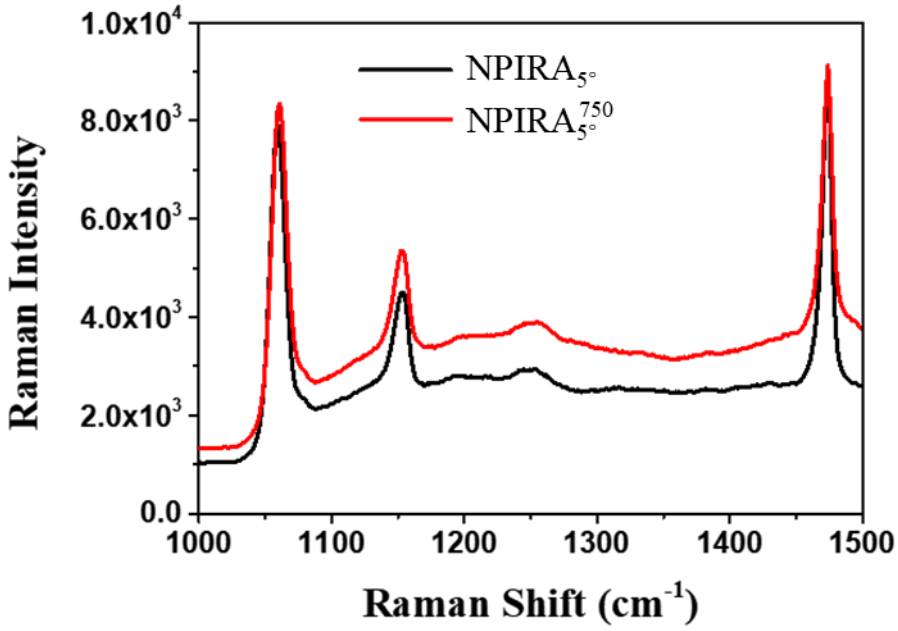

Figure S10. SERS spectra of $NPIRA_{5^\circ}$ and $NPIRA_{5^\circ}^{750}$.

REFERENCES

1. Skehan, C.; Ai, B.; Larson, S. R.; Stone, K. M.; Dennis, W.; Zhao, Y., Plasmonic and Sers Performances of Compound Nanohole Arrays Fabricated by Shadow Sphere Lithography. *Nanotechnology* **2018**, *29*, 095301.

2. Dmitriev, A.; Hägglund, C.; Chen, S.; Fredriksson, H.; Pakizeh, T.; Käll, M.; Sutherland, D. S., Enhanced Nanoplasmonic Optical Sensors with Reduced Substrate Effect. *Nano Lett.* **2008**, *8*, 3893-3898.

3. Sadowski, J. W.; Lekkala, J.; Vikholm, I., Biosensors Based on Surface Plasmons Excited in Non-Noble Metals. *Biosensors Bioelectron.* **1991**, *6*, 439-444.

4. Jin, R.; Cao, Y.; Mirkin, C. A.; Kelly, K.; Schatz, G. C.; Zheng, J., Photoinduced Conversion of Silver Nanospheres to Nanoprisms. *Science* **2001**, *294*, 1901-1903.

5. Jensen, T. R.; Malinsky, M. D.; Haynes, C. L.; Van Duyne, R. P., Nanosphere Lithography: Tunable Localized Surface Plasmon Resonance Spectra of Silver Nanoparticles. *J. Phys. Chem. B* **2000**, *104*, 10549-10556.